

Optimization of Energy Consumption and Process Sustainability in Laser Cleaning for Coating Removal

Zhihao Hou ^a, , Ziyu Tao ^{a,}, Nicolas Detalle ^a, Anthony Mannion ^a, Robert Voyle ^a*

^a Aviation Services Research Centre, The Hong Kong Polytechnic University, Hong Kong, China.

Corresponding author: Ziyu Tao

Email address: zi-yu.tao@polyu.edu.hk

Abstract: With the commercialization of laser cleaning systems, laser decoating has emerged as a robust alternative to conventional removal methods, offering advantages such as high precision, low environmental impact, and non-contact operation. However, research on optimizing the process for enhanced energy efficiency and sustainability remains limited. In this study, a pulsed Nd:YAG laser (1064 nm wavelength, 10 μ s pulse duration) was employed for decoating. Quantitative analysis identified total volatile organic compounds, carbon monoxide, and respiratory particulate matter as the primary hazardous byproducts, posing risks to operator health and the environment. To mitigate laser power absorption losses caused by the plume, computational fluid dynamics simulations using Fluent were performed to optimize the airflow design of the integrated extraction shroud. With fixed laser beam parameters, the overlap rate was investigated as a key process variable. Laboratory experiments were conducted to correlate the overlap rate with four critical factors: (1) laser source energy consumption, (2) extraction unit energy consumption, (3) respiratory particulate matter generation probability, and (4) emitted toxic gas concentrations. An objective function was then formulated by integrating the four correlations mentioned above. By minimizing this objective function, both energy efficiency and sustainability of the laser decoating process were improved simultaneously. This study proposes a practical strategy for energy conservation and emission reduction in laser decoating. Given the large-scale demand for laser decoating across industrial sectors, widespread adoption of this approach could yield significant economic and environmental benefits.

Keywords: Pulsed laser ablation; Overlap rate; Energy efficiency; Sustainability; CFD simulation; Multi-objective optimization.

1. Introduction

Laser systems have been widely adopted and studied across various fields due to their high efficiency and precision. Their applications range from laser ablation [1-4], welding [5-6], and deposition [7-8] to medical treatments [9-10]. With the commercialization of laser cleaning systems, laser ablation [11] has emerged as a robust alternative to conventional removal methods. Unlike chemical removal [12], it eliminates the need for potentially toxic and polluting organic solvents, while also avoiding substrate damage which is common drawback of mechanical grinding [13].

Laser ablation is an industrial process characterized by complex interactions [14-15] between the laser beam and the target materials. The characteristics of the laser beam [16], process parameters [13], and properties of the target materials [17] all influence the final cleaning efficiency.

Regarding the characteristics of the laser beam, important parameters include mode type (i.e., continuous wave or pulsed laser), fluence, wavelength, pulse frequency, pulse width, and diameter of the laser spot. Different laser beam characteristics can lead to various applications. For example, nanosecond (ns) and femtosecond (fs) pulsed lasers excel in precision machining [18-19]. Das and Pollock [19] investigated the microstructural characteristics of fs laser-drilled holes in thermal barrier-coated superalloys, highlighting the advantage of reduced collateral damage, such as recast layers and micro-cracking.

The influence of laser beam parameters on surface cleaning quality has been extensively studied. Burns and Cain [20] investigated the effect of pulse frequency on polymer ablation, finding a clear trend where increased pulse frequency reduced the ablation threshold using an excimer laser operating at 308 nm and 300 Hz. However, the frequency range for this phenomenon depends on the polymer's absorption coefficient. Li et al. [21] examined the cleaning process of coatings on aluminum alloys using a nanosecond pulsed laser, focusing on the effects of fluence and cleaning cycles on the morphology, element distribution, and wettability of the cleaned surface. They discovered that at a laser fluence of 19.89 J/cm², significant thermal effects were evident, with cracks and fragments remaining on the surface coating. Marimuthu et al. [22] explored the excimer laser removal of titanium nitride from coated tungsten carbide micro-milling tools, investigating the feasibility of using probe beam reflection and laser plume emission spectroscopy for online process monitoring and control. A comprehensive multi-perspective evaluation of laser

removal quality for coatings can be found in [23].

Brygo et al. [24] demonstrated the efficiency of laser ablation of paint using a nanosecond pulsed Nd:YAG laser operating at 532 nm. They investigated the laser beam parameters, including pulse frequency, laser fluence, and pulse duration. Their study revealed that the highest ablation efficiency was achieved at a frequency of 10 kHz with a fluence of 1.5 J/cm² for 100 ns pulses. Additionally, they concluded that the accumulation of particles in front of the surface at high laser pulse frequencies could decrease ablation efficiency due to the absorption and diffusion of the laser beam, indicating that effective airflow is necessary for the extraction of micro-particles. Research by Madhukar et al. [25] also found significant absorption losses of laser power in the plume generated during the paint removal process, as evidenced by plume temperature monitoring. Therefore, the airflow within the integrated shroud should be carefully designed to efficiently extract the plume, aiming for energy savings and process optimization.

Given the laser beam parameters, process factors such as laser scanning speed [26-27] and overlap rate [28] have also been reported to significantly influence surface cleaning efficiency. Additionally, the properties of the target materials play a crucial role in determining the final laser ablation efficiency. Cai et al. [29] compared the laser ablation resistance of traditional yttrium partially stabilized zirconia (YSZ) thermal insulation coating with that of a NiCrAlY/YSZ/PCS-Y₂O₃ thermal insulation/reflection-ablative coating (YPY) using a 1.07 μm YAG laser. The YPY coating demonstrated superior laser protection compared to the YSZ coating under given conditions, attributed to its high reflectivity and the laser energy consumed by PCS pyrolysis. Yang et al. [30] investigated the damage thresholds of nitride coatings with various additives and found that the laser ablation resistance of a coating primarily depended on its reflectivity.

The majority of current studies focus on optimizing the parameters of laser decoating with the goal of achieving the best surface quality [31]. Although laser decoating is an environmentally friendly cleaning method, sufficient extraction power is still required during the process to prevent the accumulation of byproducts, such as PM₁₀ and total volatile organic compounds (TVOC), which can pose health risks to operators. Furthermore, there is room for energy savings in this industrial process. In recent years, driven by the urgent need for energy conservation and environmental protection, researchers have begun to optimize the coating removal process with a

focus on reducing energy consumption [32-35]. For instance, Ouyang et al. [32-33] conducted parameter optimization targeting minimal energy consumption for both laser beam parameters (pulse widths and wavelengths) and process parameters (galvanometer scanning speed and scanning track stepover). Their research revealed that the overall energy consumption of a 355 nm wavelength laser system is significantly higher than that of a 1064 nm wavelength system. However, there has yet to be a study optimizing the laser decoating process with simultaneous goals of energy conservation and emission reduction. The plume generated during laser decoating not only causes significant absorption losses of laser power [24-25], leading to reduced energy efficiency, but also contains particulate matter that poses health threats to operators.

Therefore, it is essential to conduct further research on the laser decoating process with a focus on energy savings and emission reductions while ensuring surface cleaning efficiency. This study addresses this research gap by first performing a quantitative analysis of the byproducts generated during the laser decoating process, identifying TVOC, carbon monoxide (CO), and PM10 as the primary byproducts harmful to operator health and the environment. Next, based on this analysis, computational fluid dynamics (CFD) simulations were conducted to optimize the airflow design of the integrated extraction shroud. Finally, laboratory tests were conducted to establish individual relationships between the investigated process parameter, overlap rate, and the following four factors: laser source energy consumption, extraction unit energy consumption, PM10 generation probability, and emitted toxic gas concentration. This led to the multi-objective optimization of the laser decoating process using a common Nd:YAG laser operated at 1064 nm. The findings contribute to global energy conservation, emission reduction, and sustainable development.

2. Materials and methods

2.1 Materials and sample preparation

The specimen employed in this investigation consisted of a Ti-6Al-4V alloy plate (thickness: 1 mm) with a single-side coating application. The coating material under examination was Aerodur 2111 epoxy primer (AkzoNobel, Illinois, USA), a chromium-free corrosion-inhibiting primer specifically designed for aircraft exterior

surfaces. This urethane-compatible formulation demonstrates resistance to phosphate ester hydraulic fluids. Fig. 1 presents the cross-sectional morphology of the coated sample, acquired using a VHX-series optical microscopy system.

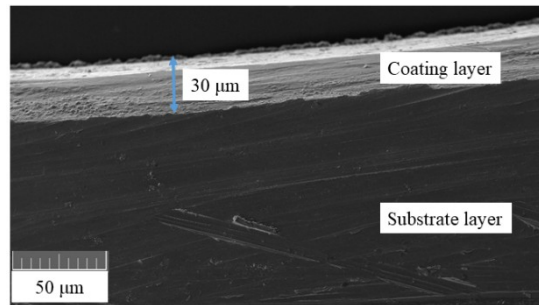


Fig. 1 Cross-sectional view of the sample.

Prior to laser removal experiments, the coating thickness was measured using an Elcometer 456 thickness gauge (range: 0–1500 μm). The reported thickness represents the average of ten measurements within the laser irradiation zone, with the corresponding standard deviation calculated for statistical reliability. Surface roughness (S_a) of the coatings was characterized via a Bruker Alicona 3D measurement system. As summarized in Table 1, the maximum inter-sample variation in coating thickness was 3.37 μm , with a low coefficient of variation ($\text{COV} = 4.29\%$). Similarly, surface roughness exhibited minimal dispersion, showing a maximum S_a difference of 0.07 μm and a COV of 3.31%. These results confirm high consistency in coating properties across all samples.

Table 1 Coating thickness and S_a of samples

Sample #	Overlap Rate (%)	Thickness (μm)		S_a (μm)	
		Mean	STD	Mean	STD
1	60	33.92	1.00	0.92	0.01
2	70	36.97	1.45	0.98	0.04
3	80	36.64	0.81	0.98	0.01
4	90	37.29	1.22	0.99	0.02

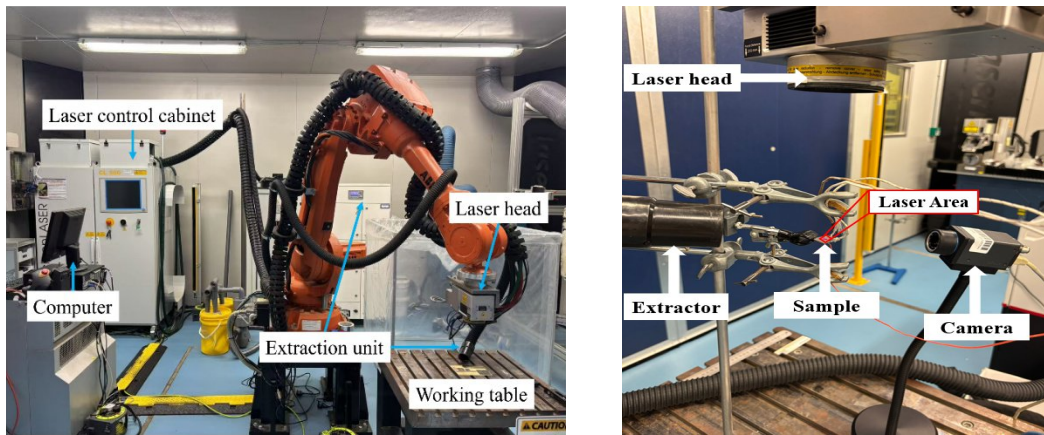
2.2 Coating removal system and scanning path

The coating removal system employed is illustrated in Fig. 2(a). A CL 500 diode-pumped solid-state laser system (Clean-Lasersysteme GmbH, Herzogenrath, Germany) was utilized for epoxy primer treatment under ambient conditions. The laser operated at a frequency of 18 kHz with a pulse duration of 10 μs and a maximum average output

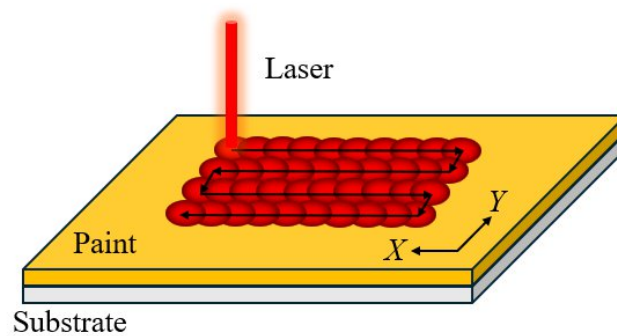
power of 250 W. The output wavelength was 1064 nm, which falls within the infrared spectrum. The focused laser spot diameter was maintained at 0.686 mm throughout the experiments. All laser treatments were conducted with exhaust ventilation at a volumetric flow rate of 500 m³/h. An enclosed shroud, whose geometry was optimally designed (as detailed in Section 3), was implemented to effectively capture particulate matter generated during the laser stripping process.

The laser scanning path configuration for coating removal is depicted in Fig. 2(b), employing uniform overlap rates in both X and Y directions. This critical parameter, i.e., overlap rate, will undergo systematic optimization in Section 5 to maximize energy efficiency and enhance process sustainability.

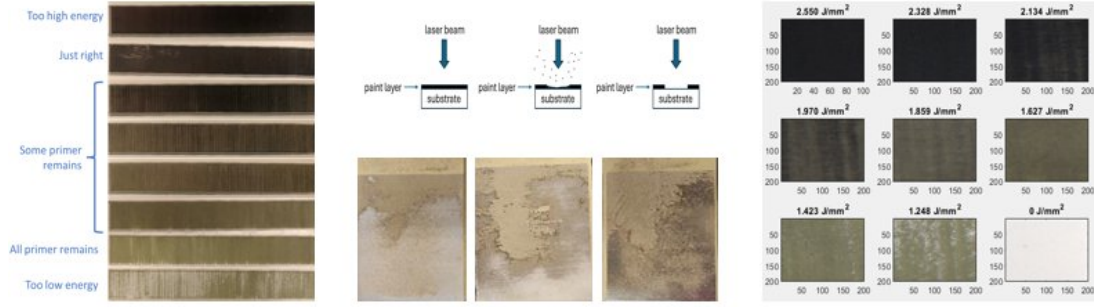
As shown in Fig. 2(c), the energy density range for better paint removal effect of the paint layer was determined through multiple experiments.



(a) Coating removal system



(b) laser scanning path



(c) laser energy density

Fig. 2 Coating removal system and laser scanning path.

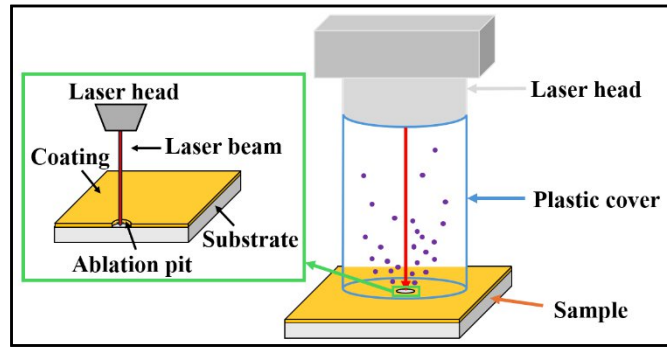
3 Byproducts collection and statistical analysis

This section focused on the collection and analysis of byproducts, particularly respirable fine particulate matter (PM) and hazardous gases. The methodologies for sampling these airborne contaminants, along with their corresponding statistical analyses, are detailed in Sections 2.3.1 (particulate matter) and 2.3.2 (gaseous emissions), respectively.

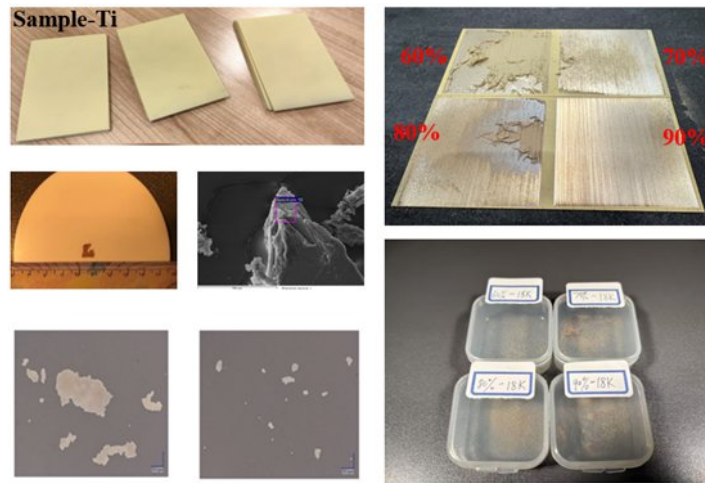
3.1 Particulate matter collection and counting

The particulate matter generated during laser decoating was collected using a sedimentation method, as illustrated in Fig. 3(a). A cylindrical plastic cover was employed to connect the laser head and sample surface during the stripping process, with the extraction system deactivated to maximize particle confinement. The laser irradiation area was maintained at $1 \text{ cm} \times 1 \text{ cm}$ to ensure sufficient particle yield for statistical analysis while preventing excessive aerosol concentration that could compromise ablation efficiency and potentially damage optical components. Following laser treatment, a one-hour sedimentation period was implemented to ensure complete particle deposition before collection using a brush.

As demonstrated in Fig. 3(b), particles collected under 60-90% laser overlap rates exhibited noticeable size distributions. Visual inspection revealed that higher overlap rates (90%) produced finer particles with noticeable agglomeration tendencies compared to lower overlap conditions.



(a) Diagram of the sedimentation method



(b) Collected particles

Fig. 3 Collection of particulate matter.

Fig. 4 presents the substrate surfaces following laser decoating at different overlap rates, demonstrating complete coating removal in a single pass for all four investigated conditions (60%, 70%, 80%, and 90% overlap). Surface roughness measurements revealed average S_a values of $0.81 \mu\text{m}$, $0.75 \mu\text{m}$, $0.89 \mu\text{m}$, and $0.83 \mu\text{m}$ for the respective overlap rates. Notably, lower overlap rates produced smoother surfaces, correlating with the observed generation of larger particulate matter (as shown in subsequent analysis). This inverse relationship between surface roughness and particle size suggests a predominance of thermal stress-induced delamination at lower overlap rates, rather than melt-dominated removal mechanisms. The reduced surface roughness at these parameters indicates minimal substrate melting and resolidification, consistent with a mechanical stripping process rather than thermal ablation.

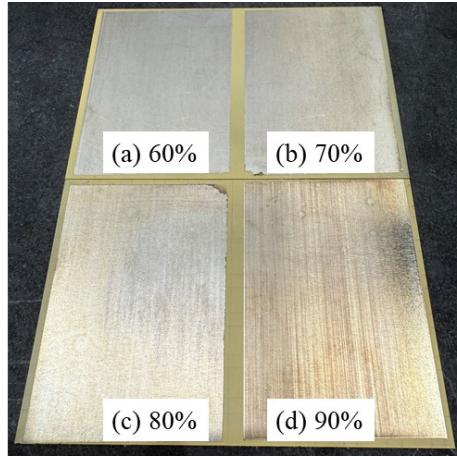
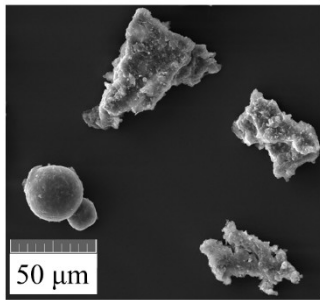
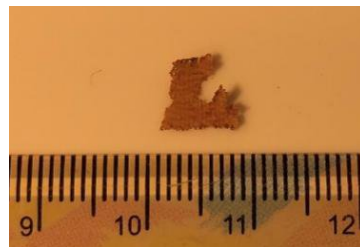


Fig. 4 Revealed substrate surface after laser de-coating.

The scanning electron micrograph in Fig. 5(a) exhibits distinct morphological features of the collected debris, including spherical resolidified molten particles and delaminated coating flakes, confirming the multi-mode removal mechanism. For the implemented 1064 nm laser system, the 10 μ s pulse duration substantially surpasses the characteristic electron-lattice thermalization time (approximate 1 ps) [36], facilitating complete conversion of absorbed photon energy into thermal energy. This thermal loading induces melting and partial vaporization of the Aerodur 2111 epoxy coating [37], resulting in material removal through concurrent mechanisms of partial vaporization, melt expulsion, and thermal stress-induced delamination [38]. Macroscopic evidence of this delamination process is presented in Fig. 5(b), showing a characteristic stripped coating section produced at 70% overlap rate, with visual correspondence to the particles shown in Fig. 3(b). Both the microscopic and macroscopic features consistently demonstrate the predominance of thermally-driven removal processes.



(a) SEM image of collected particles



(b) A large piece of stripped coating

Fig. 5 Morphology of collected particles.

Particle characterization was performed through MATLAB-based image processing of manually dispersed particulate matter, with thousands of microscopic

images acquired for analysis. Fig. 6 presents a comparative visualization of fine and coarse particles, automatically identified through grayscale threshold segmentation between particles and background. Area-equivalent diameters were statistically derived and tabulated in Table 2, revealing mean particle diameters of 9.69 μm , 9.89 μm , 7.33 μm , and 4.66 μm corresponding to overlap rates of 60% to 90%, respectively. The mean particle diameters correspond to PM10 classification, indicating potential respiratory health risks for operators [39]. It also demonstrate an inverse relationship between overlap rate and average particle size.

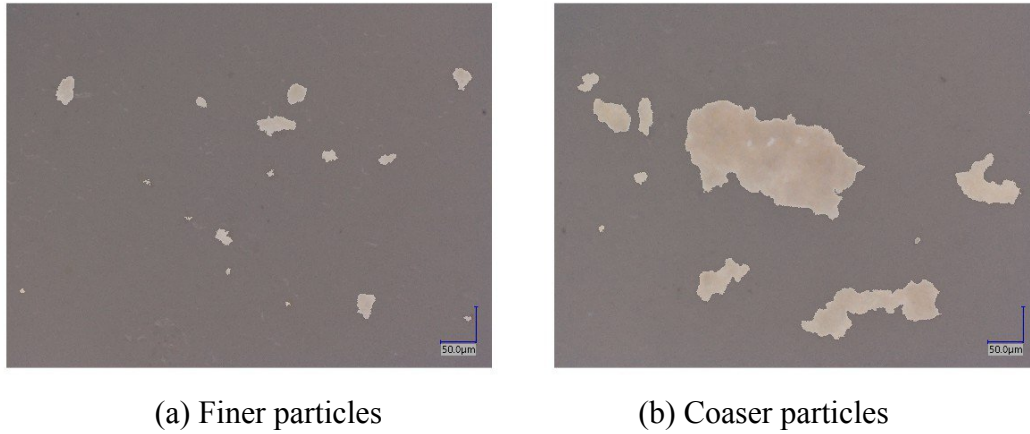


Fig. 6 Counting of particles based on image processing.

Table 2 Statistical results of particle count.

Overlap (%)	Mean (μm)	95% CI
60	9.69	[1.72, 32.29]
70	9.89	[1.72, 34.77]
80	7.33	[1.72, 25.92]
90	4.66	[1.72, 12.15]

Furthermore, the 95% confidence intervals (CI) listed in Table 2 confirm the non-uniform nature of the particle size distribution. Fig. 7 illustrates the probability density histograms of particulate matter generated at different overlap rates. The size distributions were fitted using a gamma distribution, characterized by the following probability density function (PDF):

$$f(x;a,b) = \frac{1}{\Gamma(a)b^a} x^{a-1} e^{-x/b}, x > 0 \quad (1)$$

where a and b are the shape parameter and scale parameter, respectively. $\Gamma(a)$ is the gamma function.

The goodness-of-fit for the particle size distributions was statistically validated

through Kolmogorov-Smirnov tests, yielding p-values of 5.89×10^{-28} , 3.50×10^{-54} , 5.01×10^{-60} , and 9.37×10^{-7} for overlap rates of 60% to 90%, respectively. These extremely low p-values (all well below 0.05) demonstrate statistically significant agreement between the experimental data and the fitted gamma distributions across all tested conditions.

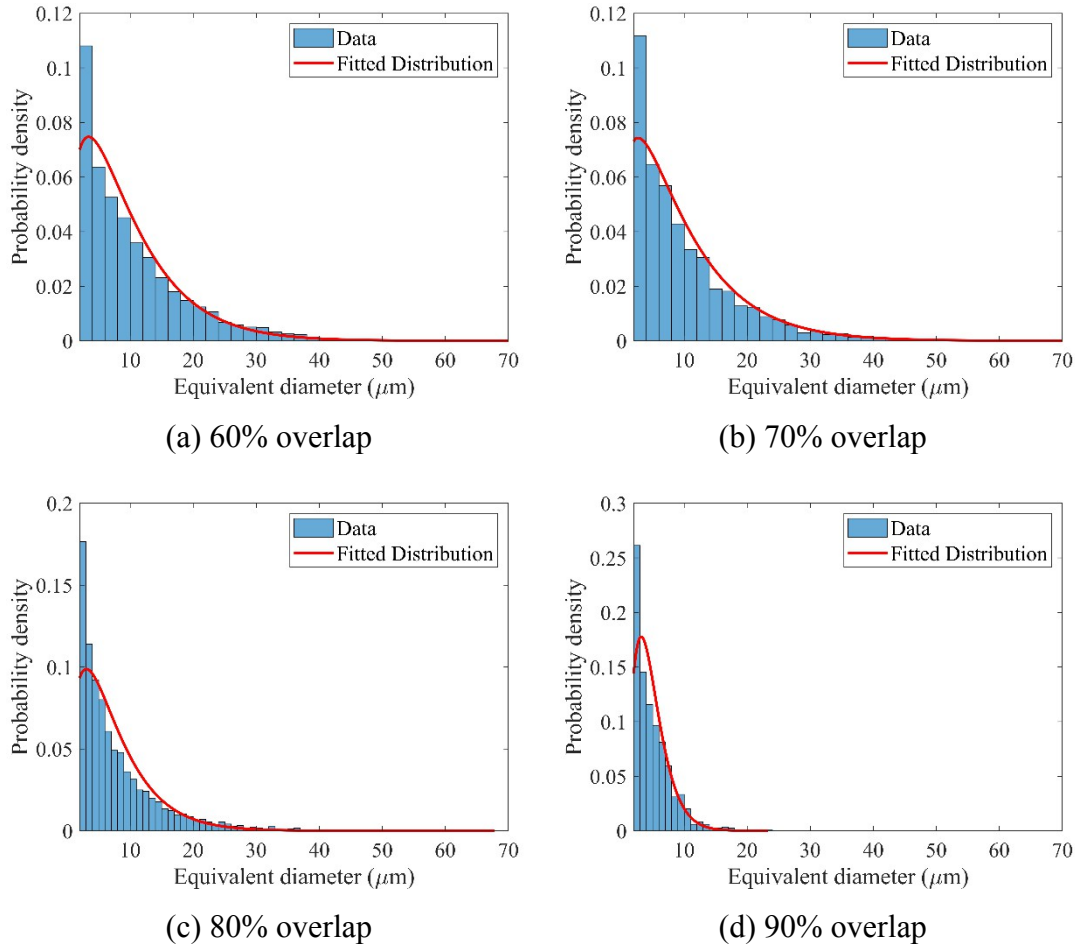


Fig. 7 Distributions of particulate matter generated by varying overlap rates

Fig. 8 presents a comparative analysis of the four PDFs for particle equivalent diameters ranging from 2 to 50 μm . The results reveal negligible differences between the fitted PDFs for 60% and 70% overlap rates. Notably, the distribution for 90% overlap rate demonstrates a pronounced shift toward finer particles, with the majority (96%) of particles exhibiting diameters below 10 μm . Quantitative analysis yields PM10 generation probabilities of 0.62, 0.62, 0.75, and 0.96 for overlap rates of 60% to 90% respectively, indicating that the 90% overlap condition presents significantly greater occupational health risks due to increased generation of respirable particulate matter. To efficiently capture the particles generated during the laser de-coating process, an enclosed shroud was optimally designed, as detailed in Section 3.

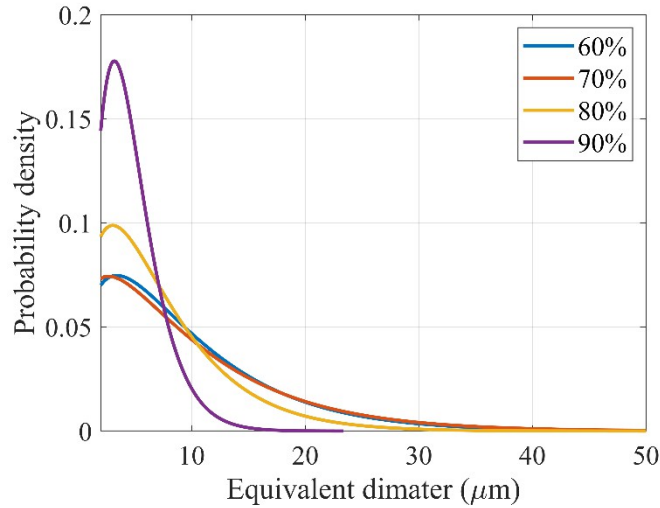


Fig. 8 Comparison of fitted PDFs for four overlap rates.

3.2 Gases collection and identification

In addition to particulate matter, toxic gases constitute another significant byproduct of the laser decoating process. Fig. 9 illustrates the gas collection setup, which consists of an enclosed chamber housing the sample. The chamber features a sliding lid with a precisely fitted opening for the laser head, which moves unidirectionally via a robotic arm. The extended length of the sliding lid ensures continuous enclosure throughout the process. A small port on the chamber body accommodates a flexible tubing system connected in series to a particle filter, an electric pump, and a gas sampling bag. To maximize the gas concentration, the pump was activated after the laser de-coating process to capture the fully mixed gaseous emissions.



Fig. 9 Diagram of the gas collection setup.

Gas composition analysis was performed using an Agilent 7890B gas chromatography-mass spectrometry (GC-MS) system equipped with headspace injection. A sample volume of 500 mL was utilized for each measurement, with duplicate analyses conducted to verify experimental reproducibility. Fig. 10(a) and 10(b) present the total ion chromatograms obtained at overlap rates of 60% and 80%,

respectively. The chromatographic profiles for 70% and 90% overlap rates exhibited similar patterns and are omitted for brevity.

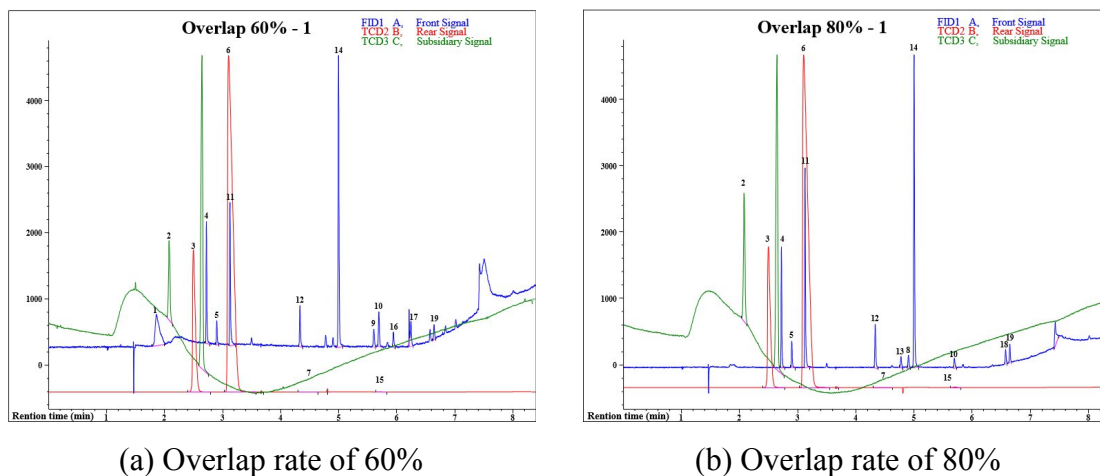


Fig. 10 Total ion chromatograms of overlap rates of 60% and 80%.

Gas chromatography-mass spectrometry analysis identified seven VOCs with potential health hazards, as summarized in Table 3: ethylene, propylene, n-butane, acetylene, cis-butene, n-pentane, and 1,3-butadiene. Time-weighted average (TWA) exposure limits further characterize their occupational health risks during prolonged operational conditions.

Table 3 Identification of toxic VOCs using GC-MS.

Peak label	Name	Molecular formula	Molar mass (g/mol)	TWA (ppm) [40-41]
11	Ethylene	C ₂ H ₄	28.05	200
12	Propene	C ₃ H ₆	42.08	200
13	n-Butane	C ₄ H ₁₀	58.12	800
14	Acetylene	C ₂ H ₂	26.04	N/A
16	Cis-2-butene	C ₄ H ₈	56.10	250
17	n-Pentane	C ₅ H ₁₂	72.15	500
18	1,3-Butadiene	C ₄ H ₆	54.09	1

The measured concentrations of TVOC across the investigated overlap rates (60-90%) ranged from 0.009% to 0.021%, with values of 0.009%, 0.012%, 0.021%, and 0.014% observed at 60%, 70%, 80%, and 90% overlap, respectively. VOC speciation analysis, as shown in Fig. 11, revealed acetylene and ethylene as the predominant components, with the 90% overlap condition exhibiting a unique compositional profile marked by maximal ethylene content (0.01%) and minimal acetylene concentration

(0.003%). Additionally, CO was identified as another significant hazardous gaseous byproduct, with concentrations measuring 0.051%, 0.069%, 0.099%, and 0.042% at the respective overlap rates.

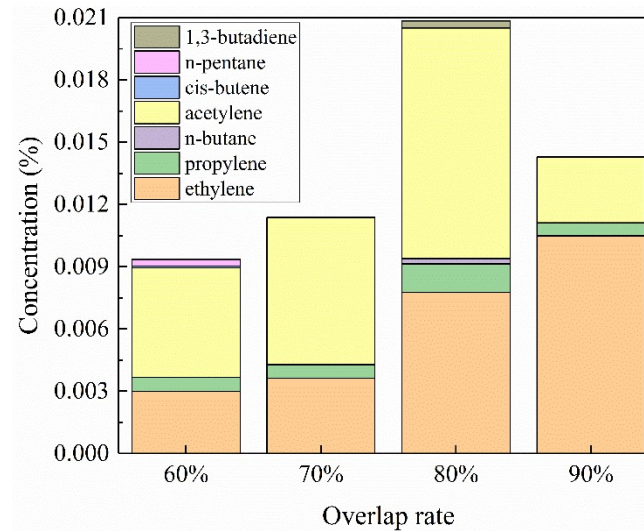


Fig. 11 Concentrations of VOCs with varying overlap rates.

4. Investigation on flow field inside integrated shroud

This paper analyzes the two-phase flow of particles and air, and the DPM-CFD model is used for simulation [42-46]. The logic diagram of the model process is shown in Fig. 12.

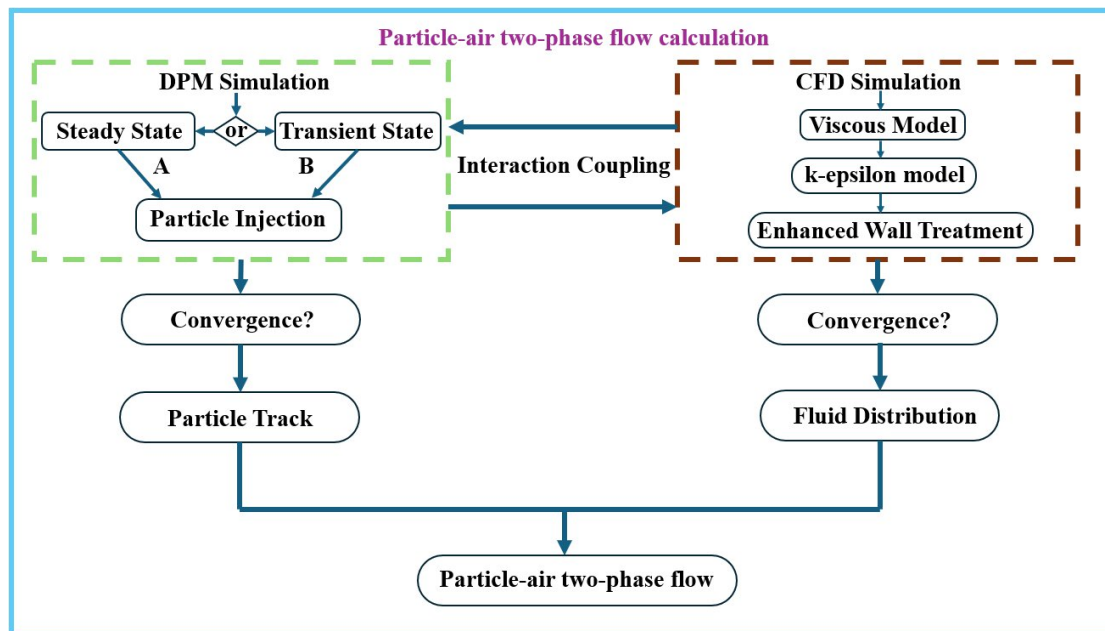


Fig. 12 Particle and air two-phase flow simulation calculation logic diagram.

3.1 Simulation methodology

SolidWorks software was used for 1:1 actual modeling. The model as a whole mainly consists of four parts: laser particle incident surface, air inlet, fluid outlet, and

wall surface. The model was meshed using hexahedrons, with a mesh size of 1mm~1.4mm, for a total of 1582173 meshes (see Fig. 13). The mesh size and number of meshes were changed, and it was verified that the calculation results of different numbers of meshes were within the allowable error range, confirming the irrelevance of the number of meshes [47].

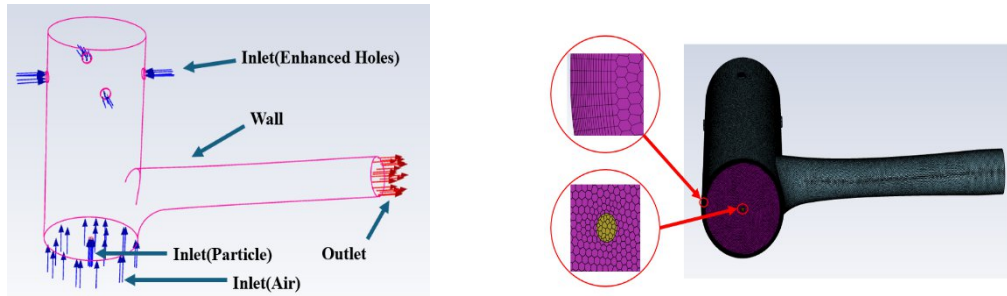


Fig. 13 CFD 3-D model & 3-D model mesh.

In this experiment, the process of particle splashing during laser ablation of paint on metal surfaces was studied. In this section, fluent simulation software is used to simulate the process, which involves the flow of particles and air.

There are four simulation methods for particle multiphase flow in fluent: 1. Euler particle flow (two-fluid model); 2.DPM model (discrete phase model); 3.DDPM model (dense discrete phase model); 4. DEM discrete element model, which is shown in Table 4. According to the experimental situation of particles, we choose the DPM model, which does not consider the collision between particles or the volume space. This model is suitable for the fluid-dominated, with particles accounting for less than 10%. It can be used to simulate the movement of small particles such as dust and aerosol. Since the continuous phase of the fluid is air, and there is no fine requirement for the fluid in the process of laser paint removal particle suction simulation analysis, we choose the standard $k-\epsilon$ model, which is shown in Table 5 [48].

Table 4 Discrete phase model of solid particles choose.

Model	Suitable particle concentration	Intergranular interaction	Calculate cost	Application scenario
Euler	High (>10%)	Y	High	Fluidized bed and pneumatic conveying
DPM	Low (<10%)	N	Low	Spray, combustion
DDPM	Middle (10%~50%)	Y	Middle	Fluidized bed, particle transport

DEM	Arbitrary (usually low)	Accurate simulation	Sky-high	Particle stacking and mixing
-----	-------------------------	---------------------	----------	------------------------------

Table 5 Fluid continuous phase model choose.

Model	Characteristic	Applicable scenario
Standard k- ϵ model	Two-equation model based on turbulent kinetic energy (K) and turbulent dissipation rate (ϵ)	General industrial flow, external flow and internal pipeline flow
RNG k- ϵ model	The improved k- ϵ model adds the statistical characteristics of small-scale turbulence.	Vortex, rotating equipment, combustion simulation
Realizable k- ϵ model	The calculation method of turbulent viscosity coefficient is improved.	External aerodynamics, complex geometric flow
Standard k- ω model	Turbulent kinetic energy (k) and specific dissipation rate (ω) are used	Boundary layer flow, low Reynolds number flow
SST k- ω model	Combining the advantages of k- ϵ and k- ω	Aircraft external flow field, automobile aerodynamics, turbine machinery
LES (large eddy simulation)	Direct analysis of large-scale turbulence and modelling of small scale	High precision research, transient flow, combustion
DNS (direct numerical simulation)	Complete analysis of turbulence at all scales	Basic research, small-scale flow

The simulation is the coupling of CFD and DPM, and attention should be paid to the setting of boundary conditions when setting initial conditions. Regarding the boundary conditions of the fluid phase, since the particles produced during laser paint removal have a certain initial velocity, we set the surface of the Inlet (particle) as a velocity inlet, and the surfaces of the other fluid inlets and outlets are all pressure-acting surfaces. Regarding the discrete phase of particles, except for the wall, the different surfaces are set to escape, which is shown in Table 6.

Table 6 Boundary condition setting of CFD and DPM.

Surface	Boundary conditions	DPM type
Inlet(Air)	Pressure-inlet	Escape
Inlet(Particle)	Velocity-inlet	Escape
Inlet(Enhanced Holes)	Pressure-inlet	Escape
Outlet	Pressure-outlet	Escape
Wall	Wall	Reflect

3.2 Model validation and optimization

This model is applied to the particle collection process after laser paint removal. We use the standard k- ϵ model as the fluid continuous phase and the DPM model as the particle discrete phase [49]. The comprehensive performance of the particle collector is evaluated based on the velocity flow field distribution and particle motion trajectory in the hood model pipeline. In order to minimize the turbulence of the fluid in the pipeline and the impact of particles on the wall (the impact of particles is divided into two parts: one is the impact on the inner wall of the pipeline, and the other is the impact damage to the laser lens located directly above the fluid inlet) [50]. After trying multiple model designs, we used two typical suction dust covers for comparative analysis [51,52]. The upper model is the version we designed at the beginning, and the lower model is the latest model after multiple rounds of optimization (see Fig. 14), and the boundary conditions of the fluid inlet and outlet are controlled to be consistent with the particle incident conditions. The simulation results show that the wind field in the upper model pipeline has a larger degree of turbulence, and the particle motion trajectory is more complicated, almost filling the inside of the dust cover. In contrast, the dust cover model below has better performance. We used transparent resin 3D printing models, conducted experiments in a dark room, used NCC green light as the light source, and used filters to reduce reflections on the model surface. The particle trajectories of the experimental results verify the correctness of the simulation model, as shown in Fig. 15.

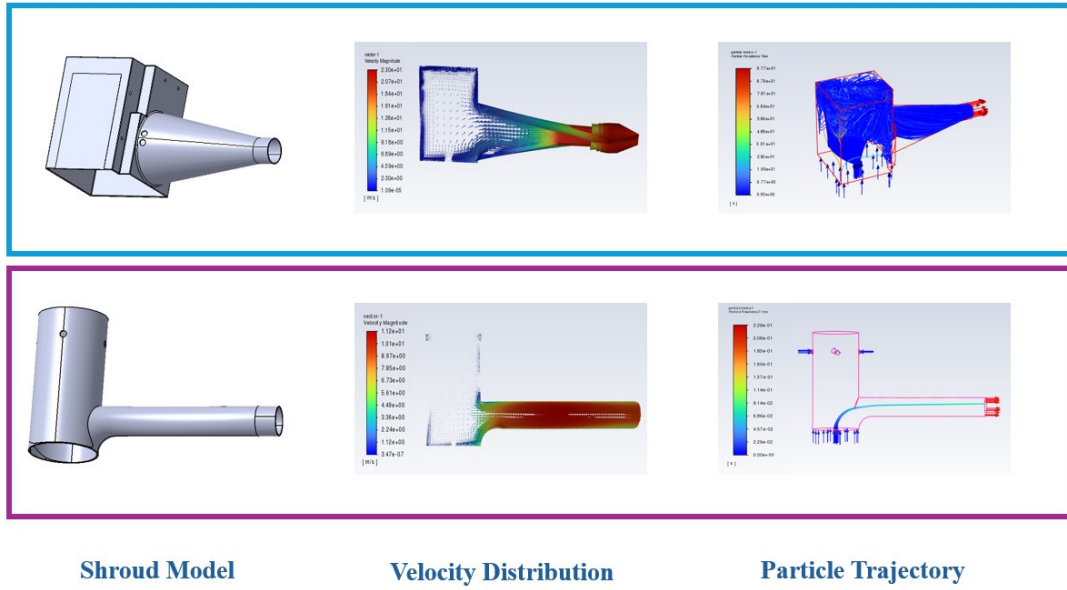


Fig. 14 Shroud model design and compare.

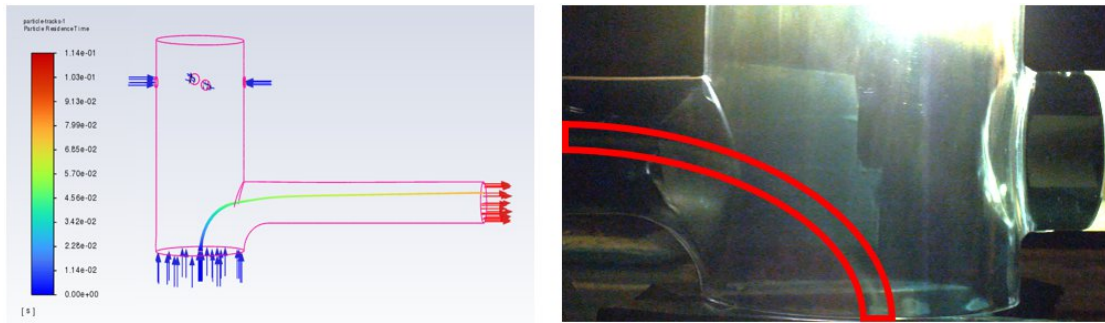


Fig. 15 Verification of simulation and experimental results.

This laser paint removal experiment is intended to be applied to large-area paint removal processes, so the particle discrete phase adopts a steady-state setting that is more in line with the actual situation. The laser paint removal process is a relatively complex process that couples multiple physical fields. At present, there is no theoretical model that can fully explain and reproduce the motion trajectory of particle splashes during laser paint removal. We focus on the collection of particles and the analysis of particle health, and do not discuss the principle of laser paint removal in detail. After consulting a large number of literature, in order to simulate the actual experimental process as accurately as possible, we adjust the incident angle of the particle incident surface to obtain the motion trajectory with relatively large changes in particle movement. When the particle incident surface is fixed, we try to change the particle incident angle (the angle between the incident direction and the fluid outlet direction), and select 30° , 90° and 150° (see Fig. 16) for comparative simulation. We can find that the latest model below is relatively small compared to the initial model above. First,

the change in the particle incident angle has a smaller impact, and secondly, the particle trajectories corresponding to different angles are more reasonable. Therefore, the latest model below can capture as many particles as possible with more incident angles [53].

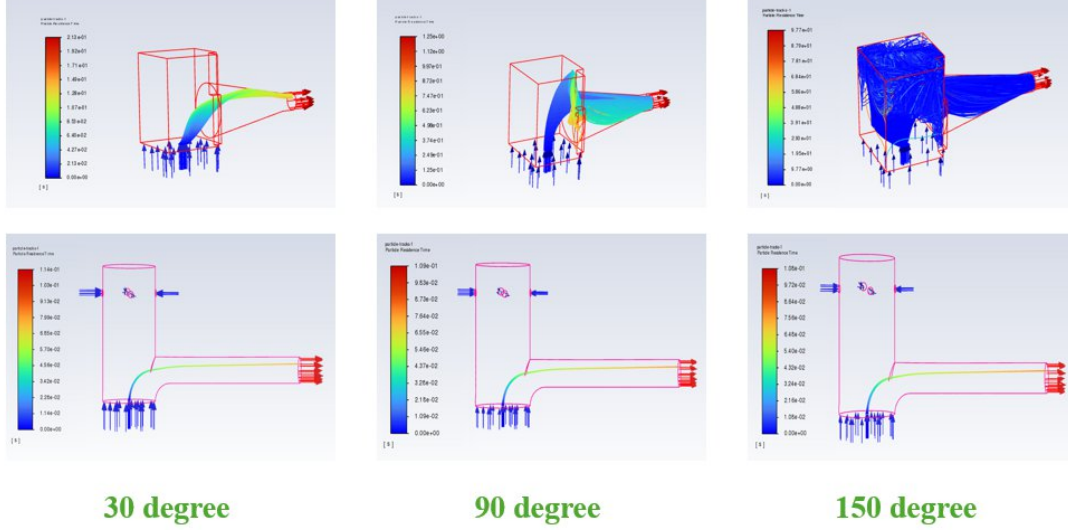


Fig. 16 Particle injection angle change.

After the dust cover model design optimization and experimental verification in this experiment, we need to further explore the particle trajectory. At this time, there are three main directions to consider: changing the particle diameter, changing the number of incident particles, and reducing the particle residence time.

In the process of simulating DPM-CFD, we use uniform distribution for the particle distribution corresponding to different laser overlap rates. Because we have found through multiple simulations of the same working conditions with only the particle distribution changed that the use of R-R distribution or uniform distribution has little effect on the capture of particle trajectories. Therefore, for the experiments in this article, the impact of the change in particle diameter can be ignored.

We achieve the change in the number of incident particles by changing the area of the particle incident surface. We selected circular incident surfaces with diameters of 5mm, 20mm, 35mm, and 50mm for simulation comparison. We found that with the increase of diameter, the particle trajectory becomes more and more complicated (it may be that the number of particles increases, the random sample space of particles increases, and the simulation results are closer to the actual situation), and the position of the particle outlet surface becomes lower and lower (it may be that the number of particles increases, agglomerates together, and the effect of gravity is more significant). In addition, the maximum residence time of particles inside the dust cover also

increases (because the particle trajectory is more complicated), as shown in Fig. 17. This simulation result further verifies that the model can well meet the complex working conditions with increasing number of particles and has practical engineering application significance.

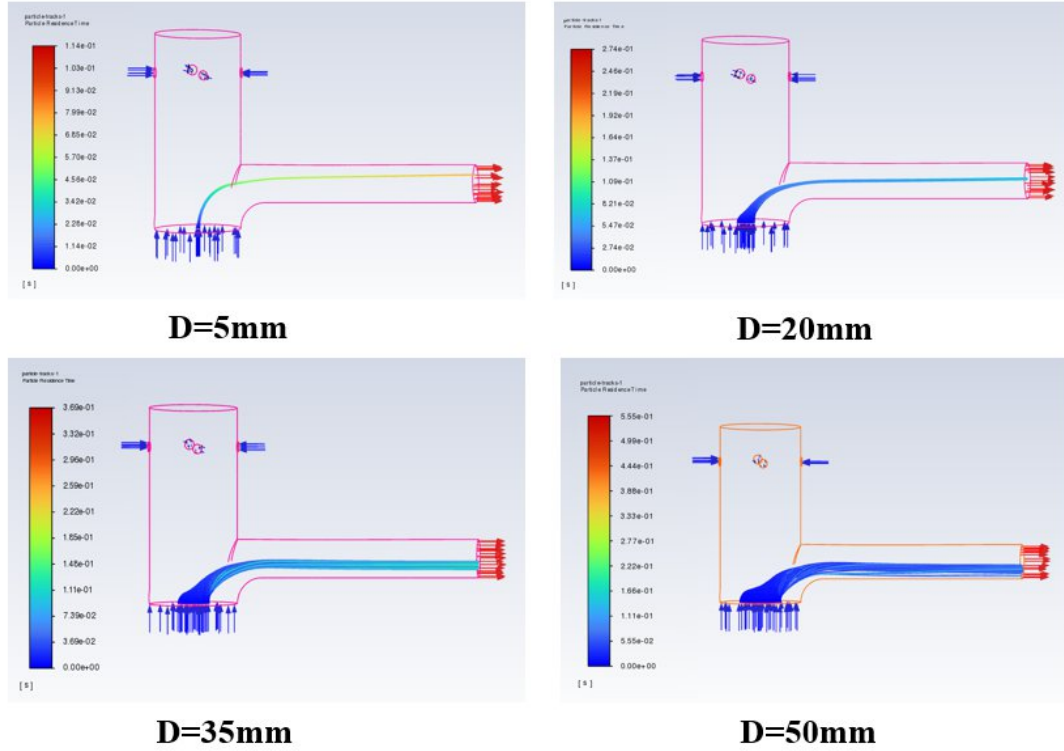


Fig. 17 Particle injection angle change.

We reduce the maximum residence time of particles in the dust cover by increasing the suction pressure on the outlet surface. In this case, the particle discrete phase uses a transient setting to better compare the suction effect. We selected three groups of outlet pressures of -60Pa, -180Pa, and -300Pa for control simulation, and selected four different instantaneous moments of 0.005s, 0.010, 0.015s, and 0.020s to view the residence position of the particles. The simulation results corresponding to three different outlet pressures: -60Pa, it takes 0.0198s for complete iteration convergence, and the particle residual rate is 27.8%; -180Pa, it takes 0.0182s for complete iteration convergence, and the particle residual rate is 11.1%; -300Pa, it takes 0.017s for complete iteration convergence, and the particles are completely extracted. And we can find that the particles remaining inside the pipe are mostly concentrated near the outlet section, which is a relatively good result. The simulation discussion in this part further verifies the correctness of the latest model we designed, as shown in Fig. 18. This simulation result shows that the model can ensure that as many particles as possible are

captured or stay in places that meet our actual requirements [54].

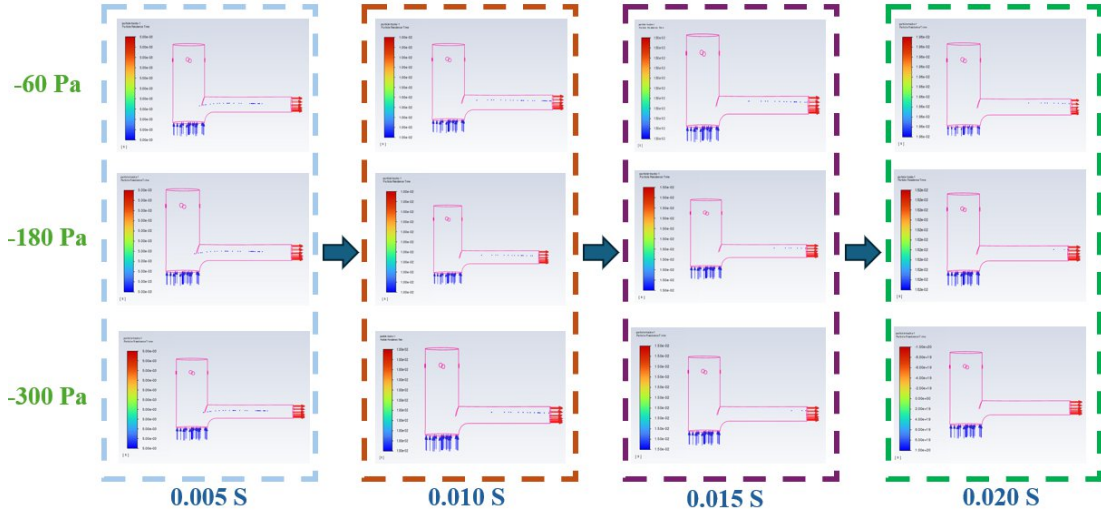


Fig. 18 Particle injection angle change.

5. Optimization of industrial laser de-coating process

This study focuses on optimizing the industrial laser de-coating process to achieve enhanced energy efficiency and improved sustainability. Fig. 19 presents a schematic overview of the proposed optimization framework. Energy efficiency is maximized through systematic reduction of power consumption from both the laser source and extraction systems. Concurrently, sustainability is addressed by mitigating occupational health risks through minimization of hazardous byproduct concentrations, specifically CO, TVOC and PM10. The final process optimization integrates these four critical objectives to establish an environmentally conscious and economically viable de-coating operation.

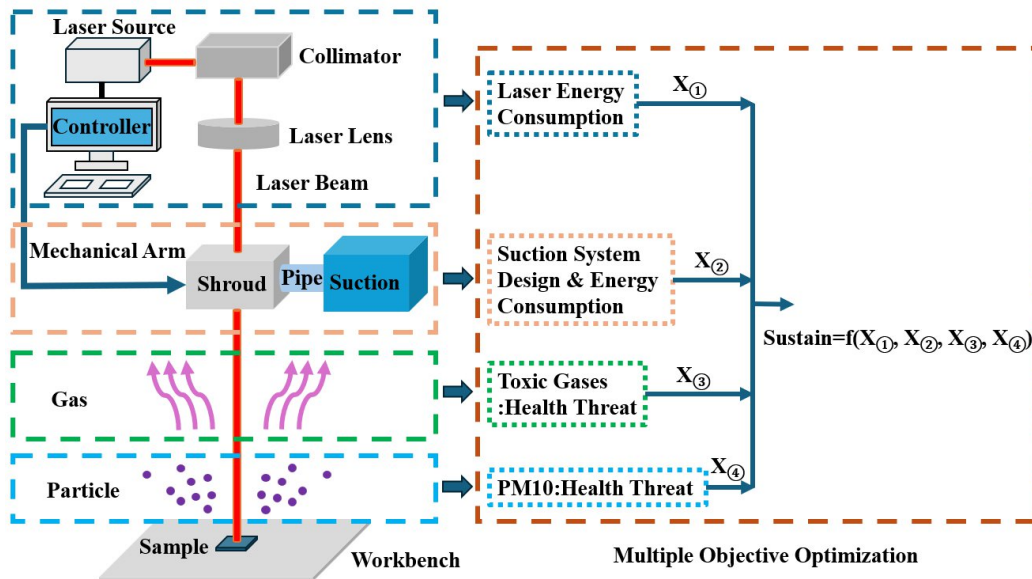


Fig. 19 Schematic representation of process optimization framework.

5.1 Energy efficiency enhancement

The energy consumption of the laser source is calculated based on the processing time and the average output power of the laser source, which is expressed as:

$$E_{laser}(\eta) = \begin{cases} \left[\frac{L_{path}}{d(1-\eta)} + 1 \right] \times \frac{1}{f} \times P_{laser}; & \eta \geq 0.7 \\ C \times \left[\frac{L_{path}}{d(1-\eta)} + 1 \right] \times \frac{1}{f} \times P_{laser}; & \eta < 0.7 \end{cases} \quad (2)$$

In Equation (2), L_{path} is the length of the coating removal area (mm). d is the laser spot diameter, which is adopted as 0.686 mm in this study. η is the overlap rate. f is the pulsed laser frequency in Hz that takes the value of 18,000 Hz in this study. P_{laser} is the average output power of the laser source with unit of Watt. Notably, the required number of passes (C) for effective coating removal exhibits a strong dependence on the overlap rate. Experimental results demonstrate that while a single pass ($C=1$) suffices for overlap rates of 70% or higher, two passes ($C=2$) are necessary at 60% overlap to achieve comparable cleaning efficacy. This threshold behavior suggests a critical transition in removal efficiency between 60% and 70% overlap conditions.

The power of the extraction unit is theoretically proportional to the product of the volumetric flow rate and the system pressure drop [55], which is defined as follows:

$$P_{ext} = Q \times \Delta p / \eta_{ext} \quad (3)$$

where Q and η_{ext} are the volumetric flow rate (m^3/s) and working efficiency of the extraction unit, respectively. Δp represents the system pressure drop (Pa) of the extraction unit.

Filters are employed within the extraction unit to capture particulate matter. This introduces an additional pressure drop to the system. The pressure drop associated with fluid flow through porous media is defined by the Ergun equation [56]. It is inferred from the Ergun equation that assuming a fixed filter porosity, the pressure drop increases with a decrease in the diameter of the particles to be captured. Assuming the filter is selected based on the mean particle diameter D_μ , the relationship between the additional pressure drop of the extraction unit and the overlap rate is obtained as follows:

$$\frac{\Delta p}{L} = 150 \frac{(1-\epsilon)^2}{\epsilon^3} \frac{\mu v}{D_\mu^2(\eta)} + 1.75 \frac{(1-\epsilon)}{\epsilon^3} \frac{\rho v^2}{D_\mu(\eta)} \quad (4)$$

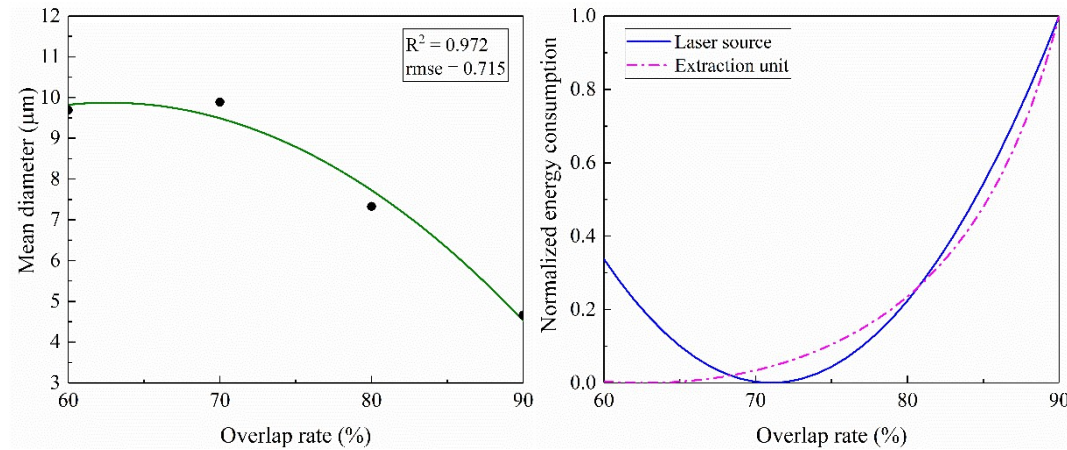
where L is the flow path length. ϵ is the porosity of the filter. μ is the air dynamic

viscosity, which was taken as $18.1 \mu\text{Pa}\cdot\text{s}$ in this study. v is the air flow velocity which was adopted as 10 m/s based on field measurements. ρ is the air density which was taken as 1.225 kg/m^3 in this study.

Table 2 had listed the mean particle diameter corresponding to each investigated overlap rate. The relationship between the overlap rate and the mean particle diameter was fitted using a second-order polynomial function, expressed as Equation (5). The fitting curve was presented in Fig. 20(a). The high R^2 value (0.972) and low root mean square error (RMSE = 0.715) demonstrate excellent agreement between the model and the experimental data.

$$D_{\mu}(\eta) = -71.75\eta^2 + 89.97\eta - 18.33 \quad (5)$$

Fig. 20(b) presents the individually min-max normalized energy consumption profiles for both the laser source and extraction unit. The laser source exhibits a direct correlation between energy consumption and total processing time, which increases with either higher overlap rates or greater repetition numbers required for complete de-coating. In contrast, the extraction unit demonstrates an inverse relationship with mean particle diameter, a behavior that originates from the particle-size-dependent pressure drop mechanism as quantified by the Ergun equation shown in Equation 4.



(a) Relationship between η and mean diameter (b) Normalized energy consumption

Fig. 20 Relationship between overlap rate and energy efficiency.

5.2 Sustainability improvement

To improve the sustainability of the laser de-coating process, the probability of PM10 generation and concentration of toxic gaseous are supposed to be minimized. Based on the laboratory tests, gamma distributions were fitted for each of the four investigated overlap rates as previously described in Section 3.1. The probability of PM10 generation is therefore readily to be obtained using the corresponding cumulative

distribution function. Concentrations of TVOC and CO were also previously introduced in Section 3.2. The quantities of byproducts of concern were consequently listed in Table 7.

Table 7 Experimental dataset for curve fitting analysis.

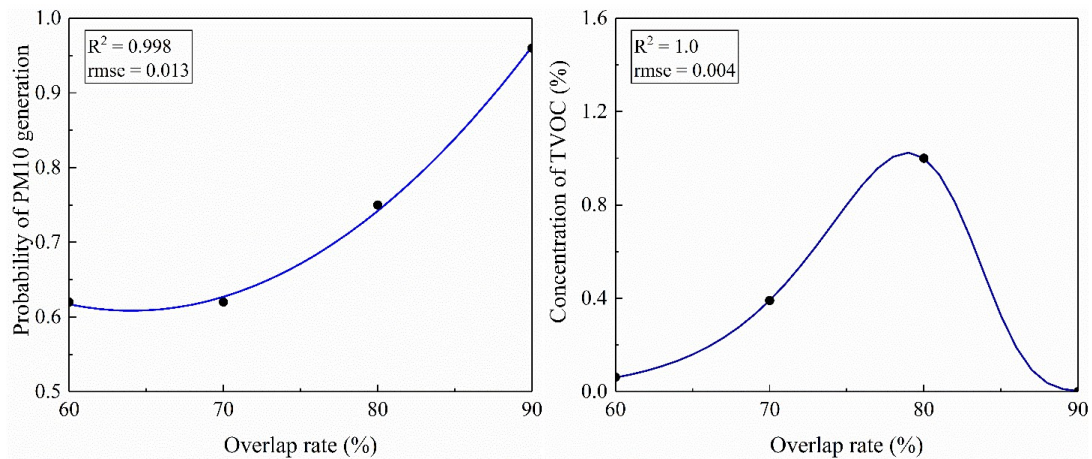
Overlap rate	Probability of PM10 generation	TVOC concentration (%)	CO concentration (%)
0.6	0.622	0.009	0.051
0.7	0.618	0.012	0.060
0.8	0.752	0.021	0.099
0.9	0.959	0.014	0.042

A second order polynomial function was adopted to fit the relationship between the overlap rate and the probability of PM10 generation, which is expressed in Equation (6). The fitting curve was shown in Fig. 21(a). The R^2 is 0.998 and the root mean square error is 0.013, demonstrating an excellent fit.

$$P_{PM10}(\eta) = 5.250\eta^2 - 6.725\eta + 2.762 \quad (6)$$

An extreme model was adopted to fit the relationship between the overlap rate and the min-max normalized total concentration of toxic gases, i.e., summation of TVOC and CO, which was expressed in Equations (7). The fitting curve was shown in Fig. 21(b). The R^2 and root mean square error were 1.0 and 0.004, respectively, representing an excellent fit.

$$C_{gas}(\eta) = 1.024 \times \exp \left[-\exp \left(\frac{\eta - 0.7896}{0.04987} \right) + \left(\frac{\eta - 0.7896}{0.04987} \right) + 1 \right] \quad (7)$$



(a) Probability of PM10 generation

(b) Normalized toxic gas concentration

Fig. 21 Relationship between overlap rate and sustainability improvement.

5.3 Multi-objective optimization of overlap rate

To enhance energy efficiency and improve sustainability of the laser decoating process, a multi-objective function was proposed as shown in Equation (8). This function is formulated by multiplying the summation of min-max normalized energy consumptions of the laser source and extraction unit by the summation of min-max normalized values of the PM10 generation probability and toxic gas concentration. It aims to minimize the objective function to achieve energy conservation and emission reduction. The variation curve of the proposed objective function with overlap rate is shown in Fig. 22, where the optimal overlap rate was identified as 68%.

$$F(\eta) = (\bar{E}_{laser}(\eta) + \bar{E}_{ext}(\eta)) \times (\bar{P}_{PM10}(\eta) + \bar{C}_{gas}(\eta)) \quad (8)$$

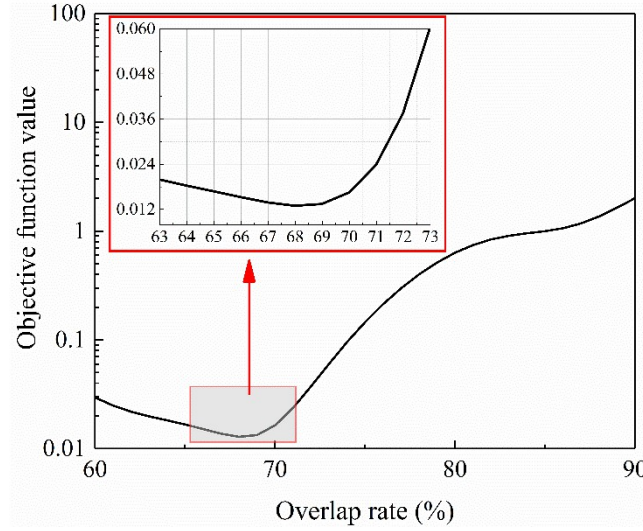


Fig. 22 Multi-objective optimization of overlap rate.

6. Conclusions

Laser decoating has emerged as a robust alternative to conventional removal methods, offering advantages such as high precision, low environmental impact, and non-contact operation. Given the large-scale demand for laser decoating across various industrial sectors, it is crucial to correlate process parameters with system energy consumption and byproduct generation to enhance energy efficiency and improve sustainability simultaneously. In this study, a pulsed Nd:YAG laser (1064 nm wavelength, 10 μ s pulse duration) was employed to clean the Aerodur 2111 epoxy primer on a Ti-6Al-4V alloy plate. The influence of overlap rate on the size distribution of generated particulate matter and concentrations of emitted toxic gases was investigated. A process optimization framework was proposed to minimize energy consumption of the laser source and extraction unit, PM10 generation probability, and

emitted toxic gas concentrations. The key findings and contributions of this research are summarized as follows:

1. For the pulsed Nd:YAG laser operated at 1064 nm and a pulse width of 10 μ s, melting and vaporization, along with stripping caused by thermal stress, are the main mechanisms for decoating.
2. Gamma distributions effectively fit the size distributions of particulate matter generated during the laser decoating process. For the case studied, PM10 generation probabilities were 62.2%, 61.8%, 75.2%, and 95.9% for overlap rates of 60% to 90%, respectively. Generally, a larger overlap rate results in smaller generated particulate matter.
3. Seven volatile organic compounds with potential health hazards were identified during the investigated laser decoating scenario: ethylene, propylene, n-butane, acetylene, cis-butene, n-pentane, and 1,3-butadiene. The emitted TVOC concentration at an overlap rate of 80% is approximately 2.3 times that at 60%.
4. A novel integrated extraction shroud was iteratively designed to optimize airflow and efficiently extract the plume generated during the laser decoating process. This optimal design protected the laser head lens and reduced absorption losses of laser energy caused by the plume.
5. An objective function was proposed that integrates the relationship between the process control variable (overlap rate) and four individual performance metrics: energy consumption of the laser source, energy consumption of the extraction unit, PM10 generation probability, and concentration of emitted toxic gases. Minimizing this nonlinear objective function can enhance energy efficiency and improve sustainability.

Although the proposed optimization framework is adaptable to various scenarios, this research focused on a single process variable, i.e., the overlap rate, due to limitations of the employed industrial laser cleaning system. Future work will expand this optimization framework to incorporate additional laser beam parameters, such as wavelength and fluence, as well as coatings with varying layers and reflectivities. Furthermore, the framework will be extended to in-field testing to examine curved samples, accounting for adjustments in laser path planning and the electrical energy consumption of other system components, such as the robotic arm's operation.

CrediT authorship contribution statement

Zhihao Hou: Writing– original draft, Visualization, Software, review & editing, Validation, Formal analysis. **Ziyu Tao**: Writing– review & editing, Methodology, Conceptualization. **Nicolas Detalle**: Writing– review & editing, Data curation. **Anthony Mannion**: Writing– review & editing, Supervision, Resources. **Robert Voyle**: Supervision, Resources, Project administration.

Declaration of competing interest

The authors declare that they have no known competing financial interests or personal relationships that could have appeared to influence the work reported in this paper.

Funding

This work was supported by the Innovation and Technology Commission (ITC) of Hong Kong SAR Government [grant number ITS/018/22FP].

Data availability

Data will be made available from the corresponding author on reasonable request.

References

- [1]. Anthofer A, Lippmann W, Hurtado A. Laser decontamination of epoxy painted concrete surfaces in nuclear plants. *Optics & laser technology*, 2014, 57: 119-128.
- [2]. Liu S, Tian Z, Shen L, et al. Numerical simulation and experimental investigation of laser ablation of Al₂O₃ ceramic coating. *Materials*, 2020, 13(23): 5502.
- [3]. Yeo C Y, Tam S C, Jana S, et al. A technical review of the laser drilling of aerospace materials. *Journal of materials processing technology*, 1994, 42(1): 15-49.
- [4]. Jia X, Chen Y, Liu L, et al. Advances in laser drilling of structural ceramics. *Nanomaterials*, 2022, 12(2): 230.
- [5]. Cao X, Wallace W, Poon C, et al. Research and progress in laser welding of wrought aluminum alloys. I. Laser welding processes. *Materials and Manufacturing Processes*, 2003, 18(1): 1-22.
- [6]. Dal M, Fabbro R. An overview of the state of art in laser welding simulation. *Optics & Laser Technology*, 2016, 78: 2-14.
- [7]. Shepelin N A, Tehrani Z P, Ohannessian N, et al. A practical guide to pulsed laser deposition. *Chemical Society Reviews*, 2023, 52(7): 2294-2321.
- [8]. Chrisey D B, Piqué A, McGill R A, et al. Laser deposition of polymer and

- biomaterial films. *Chemical Reviews*, 2003, 103(2): 553-576.
- [9]. Peng Q, Juzeniene A, Chen J, et al. Lasers in medicine. *Reports on Progress in Physics*, 2008, 71(5): 056701.
- [10]. Khalkhal E, Razzaghi M, Rostami-Nejad M, et al. Evaluation of laser effects on the human body after laser therapy. *Journal of lasers in medical sciences*, 2020, 11(1): 91.
- [11]. Li X, Wang H, Yu W, et al. Laser paint stripping strategy in engineering application: A systematic review. *Optik*, 2021, 241: 167036.
- [12]. Bonacchi D, Rizzi G, Bardi U, et al. Chemical stripping of ceramic films of titanium aluminum nitride from hard metal substrates. *Surface and Coatings Technology*, 2003, 165(1): 35-39.
- [13]. Song Y, Zhang T, Fan W, et al. Effect of the overlap ratio on surface properties of 7B04 aluminum alloy for aviation during laser derusting. *Journal of Materials Research and Technology*, 2022, 20: 1495-1511.
- [14]. Hu Y, Jiang R, Huang C, et al. Simulation and experimental study of femtosecond laser ablation mechanisms of NiCoCrAlY coatings. *Surface and Coatings Technology*, 2024, 494: 131469.
- [15]. He Z, Zheng S, Shen Y, et al. Laser-induced layer-by-layer removal and thermo-mechanical action mechanisms of FeCo-based multilayer wave-absorbing coatings. *Journal of Materials Science & Technology*, 2024, 190: 10-23.
- [16]. Bian T, Bai Y, Yang J, et al. Experimental study on laser layered removal of blue automotive paint based on optimal laser parameters. *Infrared Physics & Technology*, 2025: 105970.
- [17]. Vishnoi M, Singh V, Bansal A, et al. Effect of laser ablation over cavitation, slurry erosion, and surface properties of 86WC-10Co-4Cr based ceramic coating developed using HP-HVOLF. *Surface and Coatings Technology*, 2024, 492: 131230.
- [18]. McNally C A, Folkes J, Pashby I R. Laser drilling of cooling holes in aeroengines: state of the art and future challenges. *Materials science and technology*, 2004, 20(7): 805-813.
- [19]. Das D K, Pollock T M. Femtosecond laser machining of cooling holes in thermal barrier coated CMSX4 superalloy. *Journal of Materials Processing Technology*, 2009, 209(15-16): 5661-5668.
- [20]. Burns F C, Cain S R. The effect of pulse repetition rate on laser ablation of

- polyimide and polymethylmethacrylate-based polymers. *Journal of Physics D: Applied Physics*, 1996, 29(5): 1349.
- [21]. Li R, Feng A, Li X, et al. Study on nanosecond pulsed laser cleaning of FEP coatings on 6061-T6 aluminum alloy surface. *Optics & Laser Technology*, 2025, 187: 112798.
- [22]. Marimuthu S, Kamara A M, Whitehead D, et al. Laser removal of TiN coatings from WC micro-tools and in-process monitoring. *Optics & Laser Technology*, 2010, 42(8): 1233-1239.
- [23]. Huang X, Shen Y, He Z, et al. Multi-perspective evaluations of laser-removal quality of acrylic polyurethane coatings on aluminum alloy substrate. *Coatings*, 2023, 13(2): 359.
- [24]. Brygo F, Dutouquet C, Le Guern F, et al. Laser fluence, repetition rate and pulse duration effects on paint ablation. *Applied surface science*, 2006, 252(6): 2131-2138.
- [25]. Madhukar Y K, Mullick S, Shukla D K, et al. Effect of laser operating mode in paint removal with a fiber laser. *Applied surface science*, 2013, 264: 892-901.
- [26]. Nie J, Zhang H, Zhang D, et al. Laser-induced removal of thermal control coatings on aluminum alloy surfaces: Thermal-impact coupling effects and processes. *Applied Surface Science*, 2025: 163524.
- [27]. Zhang T, Liu T, Ban G, et al. Effect of scanning speed on laser cleaning of composite paint layer on aluminum alloy. *Optics & Laser Technology*, 2024, 171: 110470.
- [28]. Song Y, Zhang T, Fan W, et al. Effect of the overlap ratio on surface properties of 7B04 aluminum alloy for aviation during laser derusting. *Journal of Materials Research and Technology*, 2022, 20: 1495-1511.
- [29]. Cai J, Zhao F, Zhang Z, et al. Study on pyrolysis and laser ablation behavior of polycarbosilane based composite coatings on Ni-based alloy. *Journal of Alloys and Compounds*, 2023, 967: 171546.
- [30]. Yang Y, Ma Z, Rogachev A A, et al. Study on the laser ablation behavior of nitride coatings on carbon fiber epoxy resin composite. *Journal of Materials Science*, 2024, 59(1): 95-104.
- [31]. Elkaseer A, Abdelgalil I H, Lambarri J, et al. Nano-second pulsed laser ablation of inconel 718 and MMPCD for simultaneous optimal ablation rate and surface quality. *Scientific Reports*, 2024, 14(1): 31698.

- [32]. Ouyang J, Mativenga P T, Liu Z, et al. Energy consumption and process characteristics of picosecond laser de-coating of cutting tools. *Journal of Cleaner Production*, 2021, 290: 125815.
- [33]. Ouyang J, Mativenga P, Goffin N, et al. Energy consumption and performance optimisation of laser cleaning for coating removal. *CIRP Journal of Manufacturing Science and Technology*, 2022, 37: 245-257.
- [34]. Yun H, Zou B, Wang J, et al. Optimization of energy consumption in coating removal for recycling scrap coated cemented carbide tools using hybrid laser-waterjet. *Journal of Cleaner Production*, 2019, 229: 104-114.
- [35]. Chen K, Jiang X, Liu W, et al. A novel multi-objective optimization of high-power laser directed energy deposition green processes: A case study of titanium alloy. *Journal of Cleaner Production*, 2025, 494: 144877.
- [36]. Steen W M, Mazumder J. *Laser material processing*. Springer science & business media, 2010.
- [37]. *Laser ablation: principles and applications*. Springer Science & Business Media, 2013.
- [38]. Zhang Z, Yu H, Zhao S, et al. Research on the constraint of thermal stress in paint removal by pulsed laser. *Optics & Laser Technology*, 2025, 182: 112234.
- [39]. Donaldson K, Stone V, Borm P J A, et al. Oxidative stress and calcium signaling in the adverse effects of environmental particles (PM10). *Free Radical Biology and Medicine*, 2003, 34(11): 1369-1382.
- [40]. ACGIH®. (2025). *Threshold Limit Values for Chemical Substances and Physical Agents & Biological Exposure Indices*. Cincinnati, OH: American Conference of Governmental Industrial Hygienists.
- [41]. National Institute for Occupational Safety and Health (NIOSH). (2020). *NIOSH Pocket Guide to Chemical Hazards*. U.S. Department of Health and Human Services, Centers for Disease Control and Prevention.
- [42]. Zhang T., Deng S., Chen X., et al. Simulation and Analysis of Post-Mixed Abrasive Water Jet Particle Trajectory. *Journal of Chongqing University of Technology: Natural Science Edition*, 29(2), (2015)
- [43]. Wang L., Qiu X., Li J.. Mesoscale LBM-DEM model for gas-solid two-phase flow. *Chinese Journal of Computational Mechanics*, 32(5), (2015)
- [44]. Dewalle P., Vendel J., Weulersse J., et al. Characterization of Aerosols Generated by Nanosecond Laser Ablation of an Acrylic Paint. *Aerosol Science*

- and Technology, 10(40), (2010) 902-915
- [45]. Lu Y., Song W., Ang B., et al. A theoretical model for laser removal of particles from solid surfaces. *Applied Physics A: Materials Science & Processing*, (65), (1997) 9-13
 - [46]. Vereecke G., Röhr E., Heyns M.. Laser-assisted removal of particles on silicon wafers. *Journal of Applied Physics*, 7(85), (1998) 3837-3843
 - [47]. Darwin D., Richard L., George B., et al. Laser-tattoo removal—a study of the mechanism and the optimal treatment strategy via computer simulations. *Lasers in Surgery and Medicine*, 5(30), (2002) 389-397
 - [48]. Chen Z., Heng Y., Xiong P., et al. Influence of Particle Properties on the Performance and Wear of Centrifugal Pumps Based on CFD-DPM. *Journal of Xihua University: Natural Science Edition*, 43(1), (2024)
 - [49]. Peng W., Cao X.. Analysis on Erosion of Pipe Bends Induced by Liquid-solid Two-phase Flow. *Journal of Chinese Society for Corrosion and Protection*, 35(6), (2015)
 - [50]. Wang D., Feng G., Deng G., et al. Study of Mechanism on Laser Paint Removal Based on the Morphology and Element Composition of Ejected Particle. *Chinese Journal of Lasers*, 42(10), (2015) 1003007
 - [51]. Ma X., Zhong W.. CDF-DPM Simulation on the Atmospheric Pollutant Dispersion in Industrial Park. *Atmosphere*, 15(3), (2024) 030298
 - [52]. Razab M., Jaafar M., Rahman A., et al. Study of Health Implications Effects in Laser Paint Removal Process Based on PM 1.0 and PM 10.0 Measurements. *Journal of Tropical Resources and Sustainable Science*, (2), (2014) 30-39.
 - [53]. Hao X., Yu X., Liu Z., et al. The application of response surface methodology in optimization of microbial media. *Food Research and Development*, 27(1), 2006 38-41.
 - [54]. Gui J., Kang H.. Response surface method for structural reliability analysis and its realization with Matlab. *Chinese Journal of Computational Mechanics*, 21(6), (2004) 683-687.
 - [55]. Dukhan N, Patel P. Equivalent particle diameter and length scale for pressure drop in porous metals. *Experimental Thermal and Fluid Science*, 2008, 32(5): 1059-1067.
 - [56]. Macdonald I F, El-Sayed M S, Mow K, et al. Flow through porous media-the

Ergun equation revisited. Industrial & Engineering Chemistry Fundamentals, 1979, 18(3): 199-208.